Journal of Geodesy (2002) 76: 150–168
DOI 10.1007/s00190-001-0227-4

Journal of Geodesy

Computing components of the gravity field induced by distant topographic masses and condensed masses over the entire Earth using the 1-D FFT approach

D. A. Smith

NOAA/National Geodetic Survey, 1315 East–West Highway, Silver Spring, MD 20910, USA
e-mail: dru.smith@noaa.gov; Tel.: + 1-301-713-3202; Fax: + 1-301-713-4172

Received: 13 December 2000 / Accepted: 3 September 2001

Abstract. A new method for computing gravitational potential and attraction induced by distant, global masses on a global scale has been developed. The method uses series expansions and the well known one-dimensional fast Fourier transform (1-D FFT) method. It has been proven to be significantly faster than quadrature while being equally accurate. Various quantities were studied to cover the two primary applications of the Stokes–Helmert scheme of modeling effects. These two applications (or paths), given the names R/r/D and R/D/r, are briefly discussed, although the primary objective of the paper is to provide computational information to either path, rather than choosing one path as preferable to the other. It is further shown that the impact of masses outside a 4-degree cap can impact the absolute computation of the geoid at more than 1 cm, and should therefore be included in all local geoid computations seeking that accuracy.

1 Introduction

In many physical geodesy applications, especially the Stokes–Helmert approach to geoid modeling (Martinec 1998; Vaníček et al. 1998; Smith and Roman 2001a), it is necessary to compute various components of the gravitational field due to the Earth's masses above the geoid (in both their true and condensed forms). There have been various studies on this issue in the last few years (Sjöberg and Nahavandchi 1999; Sjöberg 2000; Smith et al. 2001). Due to the exponential nature of the kernel function in Newtonian potential and gravitational kernels, it is often advantageous to treat 'far' masses in a different computational manner than 'near' masses. Previous studies of 'far' mass effects concentrated primarily on spherical harmonic approaches. (Nahavandchi and Sjöberg 1998; Sjöberg and Nahavandchi 1999; Nahavandchi 2000; Sjöberg 2000). This paper presents a different method for computing a variety of useful components of the gravity field induced by 'far' masses through the use of the well-known one-dimensional fast Fourier transform (1-D FFT) approach (Haagmans et al. 1993, Smith and Milbert 1999).

In addition to computing quantities on a coarse (e.g. 5-arcminute) global grid, a useful method of combining such a coarse grid with local fine (e.g. 1-arcsecond) grids is presented. In this way global 'outer-zone' effects can be computed at locations on a detailed Digital Elevation Model (DEM) grid. Furthermore, this means that a re-computation of gravitational attraction and potential due to an updated high-resolution local DEM can be done quickly, without needing to re-run the FFT procedure itself.

2 'Helmertization' of the topography

In the Stokes–Helmert solution to the fundamental boundary value problem of physical geodesy, the masses of the Earth are mathematically manipulated (using Helmert's 2nd method of condensation) so that no masses lie external to the geoid. This causes a complex, but computable, change to both the gravitational potential and gravitational attraction fields (presuming knowledge of the topographic density). A discussion of some attributes of Helmert's 2nd condensation method can be found in Heiskanen and Moritz (1967) and Wichiencharoen (1982). The answer to which components of the potential and attraction fields are needed depends on the order of events chosen when applying the Stokes–Helmert scheme (see Appendix). In Fig. 1, a simple schematic shows the ellipsoid, geoid and topography before any application of Helmert's 2nd method of condensation, or 'Helmertization', of the topography ('Helmertization' as used here means the 3-D masses have been removed, and a 2-D condensed mass layer on the geoid has been added, where the condensation occurs along the local vertical). Gravity measurements are taken (and anomalies can be computed) at point P on the surface of the Earth. Figure 2 shows the final goal needed in order to apply the Stokes–Helmert scheme,

with the 3-D masses above the geoid replaced with a 2-D mass layer on the geoid, and point P_0 is vertically below point P, and located on the geoid. Gravity values (and ultimately gravity anomalies) are needed at point P_0 in this 'Helmert space' (Vaníček et al. 1998). There are an infinite number of ways to mathematically manipulate the masses so that one arrives at Fig. 2 from Fig. 1. However, only two are frequently used in application. These two cases will be referred to as R/r/D and R/D/r. These acronyms will be explained in the following paragraphs.

2.1 The R/r/D method

Vaníček et al. (1998) apply the Stokes–Helmert method by performing the following gravity reductions, in this order

(1) Remove the topographic masses (step 'R').
(2) Restore the condensed masses on the geoid (step 'r').
(3) Downward continue from P to P_0 (step 'D').

This method is graphically displayed in the left column of Fig. 3.

2.2 The R/D/r method

Another way of applying the Stokes–Helmert method is to perform gravity reductions in the following order, slightly different from that of the R/r/D method.

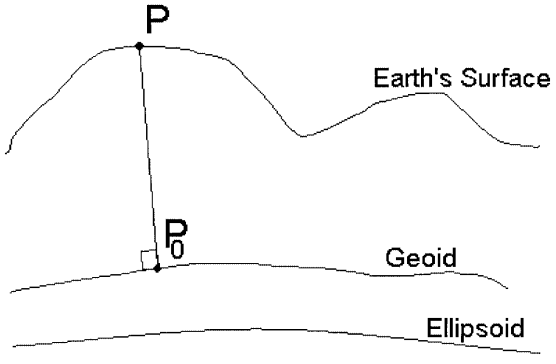

Fig. 1. The Earth before 'Helmertization' of the terrain

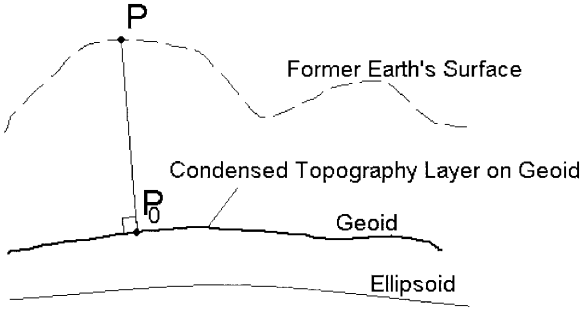

Fig. 2. The Earth after 'Helmertization' of the terrain (in 'Helmert space')

(1) Remove the topographic masses (step 'R').
(2) Downward continue from P to P_0 (step 'D').
(3) Restore the condensed masses on the geoid (step 'r').

This method is graphically displayed in the center column of Fig. 3.

It should be pointed out that the use of '(R)emove' and '(r)estore' in this paper should not be confused with other 'remove/restore' methods [such as the removal and restoration of long-wavelength information to bandwidth limit data going through an FFT process].

2.3 Other methods

In addition to the R/r/D and R/D/r methods, one can achieve gravity on the geoid in Helmert space in other ways. One such method, D/R/r, is illustrated in the right column of Fig. 3. While such a method will achieve the same goal as the R/r/D and R/D/r methods, its practical application is almost impossible to achieve due to the difficulty in accurately computing the downward continuation of gravity *through* the topographic masses. As such, it is presented only for the sake of curiosity and will not be pursued further in this paper.

2.4 On the order of events

The two methods of acquiring gravitational attraction (which will lead to gravity anomalies) at P_0 in Helmert space shown in Sects. 2.1 and 2.2 (R/r/D and R/D/r) are different but achieve exactly the same goal. Milbert and Smith (1998) have shown the equivalence of R/r/D and R/D/r (and, in fact, D/R/r) using an analytical (spherical) model of the Earth. A formal, and general, proof of the mathematical equivalence of R/r/D and R/D/r is given in the Appendix of the present paper. The point here is that while the R/r/D and R/D/r methods yield the same value of Helmert gravity (mathematically speaking – the actual implementation of R/r/D and R/D/r may yield numerically different results due to numerical methods used, round-off error, etc.), the potential and attraction components (induced by the topography) needed for the R/r/D path are slightly different than those for the R/D/r path. The necessary quantities are shown in Fig. 3, but stated explicitly below.

In the R/D/r path, the following components are needed.

(1) The gravitational attraction of 3-D topographic masses computed at P (the surface of the Earth), ${}_T g_P$.
(2) The gravitational attraction of 2-D condensed topographic masses computed at P_0 (the geoid), ${}_C g_{P_0}$.

In the R/r/D path, the following components are needed.

(1) The gravitational attraction of 3-D topographic masses computed at P (the surface of the Earth), ${}_T g_P$.
(2) The gravitational attraction of 2-D condensed topographic masses computed at P (the surface of the Earth), ${}_C g_P$.

The difference, obviously, is in the 2nd component of each path. The R/D/r path needs ${}_{C}g_{P_0}$ while the $R/r/D$ path requires ${}_{C}g_{P}$. [Of course, for the two paths to yield identical results, they will obviously have different downward-continuation (DC) computations. This can be seen mathematically in the Appendix, but the method of computing the DC terms is not addressed in this paper. It should be noted that numerical differences in the DC computations might yield different values of Helmert gravity, even though the R/r/D and R/D/r methods are mathematically equivalent.]

In both cases, for computing the indirect effect, it is necessary to know the change in potential at the geoid due to the Helmertization of the topography. That is, one needs to know the following.

(1) The gravitational potential of 3-D topographic masses computed at P_0 (the geoid), ${}_{T}W_{P_0}$.

(2) The gravitational potential of 2-D condensed topographic masses computed at P_0 (the geoid) ${}_{C}W_{P_0}$.

3 Requirements of the 1-D FFT approach

In order to facilitate the use of the spherical 1-D FFT method, all integrals for potential or gravitational attraction, whether induced from 3-D masses or 2-D (condensed masses) and whether computed at the Earth's surface or at the geoid, will be manipulated so that they are either one double integral (in f and l) or a sum of double integrals, but where each double integral must be a *convolution in longitude*. Each such a convolution integral in longitude will follow the following general formula:

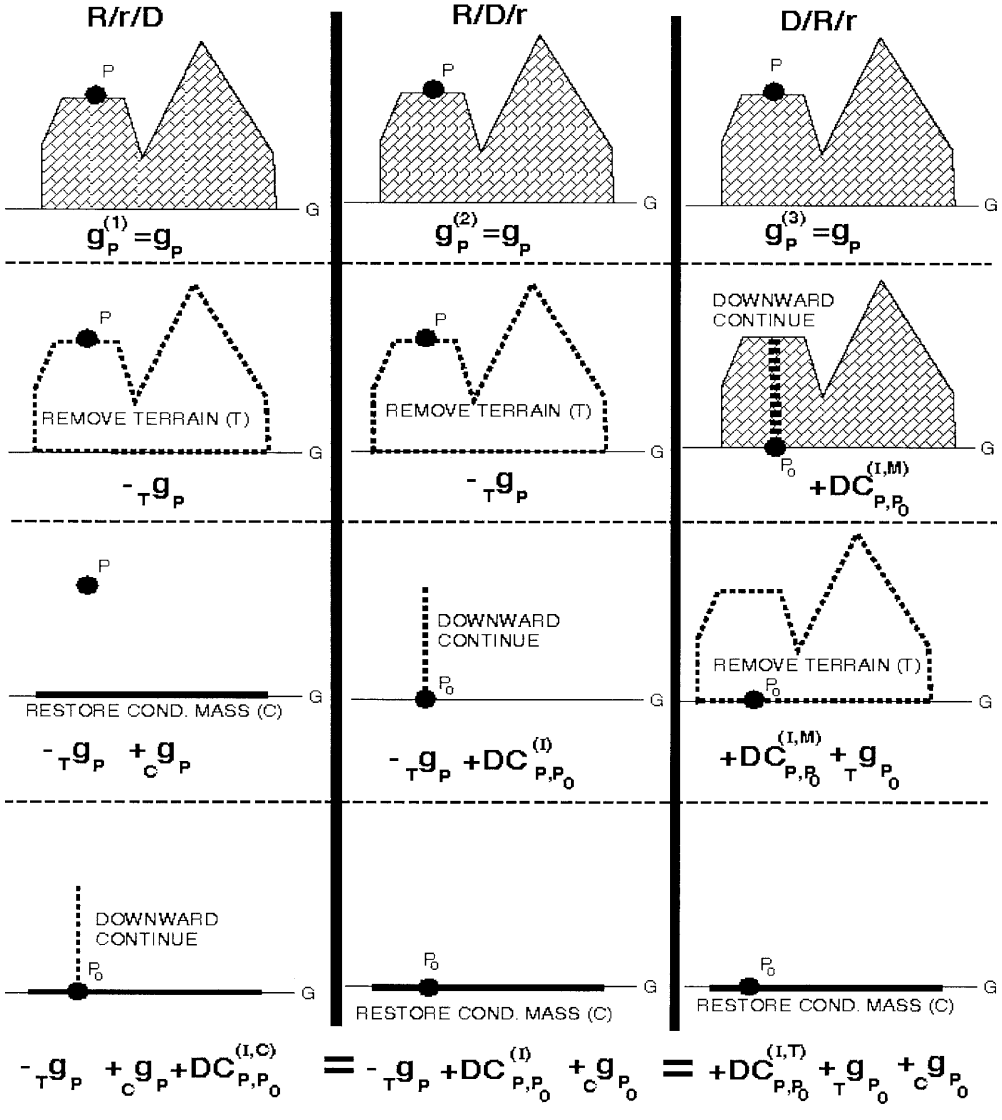

Fig. 3. The R/r/D, R/D/r and D/R/r methods of Helmertization

$$f_1(\phi_P, \lambda_P, r_P) = k \int_{\phi=-\pi/2}^{\pi/2} \int_{\lambda=0}^{2\pi} f_2(\phi, \lambda) f_3(\phi, \phi_P, \lambda - \lambda_P) \cos\phi \, \mathrm{d}\lambda \, \mathrm{d}\phi \tag{1}$$

where
ϕ, λ = latitude and longitude of roving integral point
ϕ_P, λ_P = latitude and longitude of station
k = any constants with no dependence on ϕ, λ, ϕ_P, nor λ_P.

Because the integrals in Eq. (1) are convolutions in longitude (between $f_2 \cos\phi$ and f_3) they may be solved efficiently and accurately using well-known 1-D FFT techniques (Haagmans et al. 1993)

$$F_{1,\varphi_i}(\lambda_i) = k\Im^{-1}\left[\sum_{\phi_j=\phi_1}^{\phi_n} \Im(f_{3,\phi_j}(\Delta\lambda_{i,j}))\Im(f_{2,\phi_j}(\lambda_j)\cos\phi_j)\right] \tag{2}$$

The manipulation of gravitational potential and gravitational attraction integrals into convolutions is presented in the next section.

4 Gravitational integrals for 2-D and 3-D topographic masses

As mentioned previously, this paper discusses five different components of the potential and attraction fields induced by the topography in the Stokes–Helmert scheme (various ones of which are used depending on what 'path' one takes to 'Helmertize' the topography). Each of these components is expounded in a separate section below.

4.1 Gravitational attraction of 3-D masses computed at the Earth's surface ($_Tg_P$)

Begin with the gravitational potential (W) at a point P on the Earth's surface (r_P, ϕ_P, λ_P) generated by the 3-D topography (T). This is written as (Heiskanen and Moritz 1967, p. 3)

$$_TW_P = {}_TW(r_P, \phi_P, \lambda_P) = \int_V \frac{G}{l}\rho \, \mathrm{d}V \tag{3}$$

where G is the Universal gravitational constant, V is the volume of the 3-D topography, $\rho \, \mathrm{d}V$ is a differential mass element (density times differential volume element), and l is the distance between P and $\rho \, \mathrm{d}V$. This equation can be expanded more formally as

$$_TW_P = \int_\varphi \int_\lambda \int_r \frac{G\rho}{l} \mathrm{d}V = \int_\varphi \int_\lambda \int_r \frac{G\rho}{l} r^2 \cos\varphi \, \mathrm{d}r \, \mathrm{d}\lambda \, \mathrm{d}\varphi \tag{4}$$

where $\mathrm{d}V$ is a differential volume element, ρ is the density at $\mathrm{d}V$ and the distance l can be written as

$$l = \sqrt{r^2 + r_P^2 - 2rr_P\cos\psi} \tag{5}$$

where r and r_p are the geocentric distances to $\mathrm{d}V$ and P respectively. The angle ψ is the angle formed by connecting the Earth's geocenter with $\mathrm{d}V$ and P. Combining this information, one has

$$_TW_P = \int_\varphi \int_\lambda \int_r \frac{G\rho r^2}{\sqrt{r^2 + r_P^2 - 2rr_P\cos\psi}} \cos\varphi \, \mathrm{d}r \, \mathrm{d}\lambda \, \mathrm{d}\varphi \tag{6}$$

If one is interested in the gravitational attraction of the topographic masses at $P(_Tg_P)$, then the radial derivative of potential must be taken

$$_Tg_P = {}_Tg(r_P, \varphi_P, \lambda_P) = -\frac{\partial_T W_P}{\partial r_P} \tag{7}$$

Combining the above two equations yields

$$_Tg_P = \int_\varphi \int_\lambda \int_r \frac{G\rho r^2 (r\cos\psi - r_P)}{\left[\sqrt{r^2 + r_P^2 - 2rr_P\cos\psi}\right]^3} \cos\varphi \, \mathrm{d}r \, \mathrm{d}\lambda \, \mathrm{d}\varphi \tag{8}$$

The integral with respect to r can be solved analytically [see also Martinec 1998, Eq. (3.54)], leaving a double integral in ϕ and λ

$$\begin{aligned} _Tg_P = \int_\varphi \int_\lambda G\rho \Bigg[& \frac{6rr_P\cos^2\psi - rr_P - \cos\psi\left(r^2 + 3r_P^2\right)}{\sqrt{r^2 + r_P^2 - 2rr_P\cos\psi}} \\ & + \left(r_P - 3r_P\cos^2\psi\right) \\ & \times \ln\left(r - r_P\cos\psi + \sqrt{r^2 + r_P^2 - 2rr_P\cos\psi}\right)\Bigg]_{r=r_1(\varphi,\lambda)}^{r=r_2(\varphi,\lambda)} \\ & \times \cos\varphi \, \mathrm{d}\lambda \, \mathrm{d}\varphi \end{aligned} \tag{9}$$

If we assume for now that the geoid is a sphere of constant radius 'R', then we may state the following:

$$\begin{aligned} r_1 &= R \\ r_2 &= R + H(\varphi, \lambda) \\ r_P &= R + H_P \end{aligned} \tag{10}$$

The spherical assumption ($r_1 = R$) is important for the simplicity of the remaining equations of this paper. More rigorous assumptions should eventually be tried (geoid = ellipsoid or even geoid = 'high-resolution global geoid model') to obtain more accurate values of distant topographic effects, and reduce any long-wavelength errors due to the differences between a sphere, ellipsoid and geoid.

The equation for ψ shows the dependence on ϕ, ϕ_P and $\lambda - \lambda_P$

$$\cos\psi = \sin\varphi\sin\varphi_P + \cos\varphi\cos\varphi_P\cos(\lambda - \lambda_P) \tag{11}$$

For the purposes of discussion, Eq. (9) can be written compactly as

$$ {}_T g_P = \int_{\varphi} \int_{\lambda} G\rho\{f[R, H_P, H(\varphi,\lambda), \psi(\varphi,\varphi_P,\lambda-\lambda_P)]\} \times \cos\varphi \, \mathrm{d}\lambda \, \mathrm{d}\varphi \quad (12) $$

It stands to reason, therefore, that if the variables H_P, H and ψ could be separated from one another in function f so that H_P could be brought outside the integral, and only products of H and ψ remained, one would have a convolution in longitude in the manner of Eq. (1). However, this is not possible as Eq. (12) stands. It is possible, though, to expand f into an infinite power series in H and H_P. Such a series is written

$$ \begin{aligned} f(R, H_P, H, \psi) &= \sum_{j=0}^{\infty} \sum_{i=0}^{\infty} H_P^j H^i w_{i,j} \\ &= \sum_{j=0}^{\infty} \sum_{i=0}^{\infty} H_P^j H^i(\varphi,\lambda) w_{i,j}(R,\psi) \\ &= \sum_{j=0}^{\infty} H_P^j \sum_{i=0}^{\infty} H^i(\varphi,\lambda) w_{i,j}(R,\psi) \end{aligned} \quad (13) $$

Combining Eqs. (12) and (13) one arrives at

$$ {}_T g_P = \int_{\varphi} \int_{\lambda} G\rho \sum_{j=0}^{\infty} H_P^j \sum_{i=0}^{\infty} H^i w_{i,j} \cos\varphi \, \mathrm{d}\lambda \, \mathrm{d}\varphi \quad (14) $$

Then, pulling the constants out of the integral, and rearranging summations and integrations, yields

$$ {}_T g_P = G\rho \sum_{j=0}^{\infty} H_P^j \sum_{i=0}^{\infty} \int_{\varphi} \int_{\lambda} H^i w_{i,j} \cos\varphi \, \mathrm{d}\lambda \, \mathrm{d}\varphi \quad (15) $$

Note that density (ρ) has been assumed constant in these equations. Any variation in ρ (based on ϕ, λ or H) would require re-formulating Eq. (15). Now each integral in Eq. (15) is a convolution in longitude, and subject to solution through the use of 1-D FFT methods. The various $w_{i,j}$ kernel functions (to $i = j = 4$) are as follows:

$$ \begin{aligned} &w_{i,j} = 0 \quad \forall\, i = 0 \\ &w_{1,0} = \frac{1}{2\sqrt{2}(1-c)^{1/2}} && w_{3,0} = \frac{-7+3c}{48R^2\sqrt{2}(1-c)^{3/2}} \\ &w_{1,1} = -\frac{1-3c}{4R\sqrt{2}(1-c)^{3/2}} && w_{3,1} = \frac{7-34c-9c^2}{96R^3\sqrt{2}(1-c)^{5/2}} \\ &w_{1,2} = \frac{-3-15c}{16R^2\sqrt{2}(1-c)^{3/2}} && w_{3,2} = \frac{47+94c+15c^2}{128R^4\sqrt{2}(1-c)^{5/2}} \\ &w_{1,3} = \frac{13+10c-35c^2}{32R^3\sqrt{2}(1-c)^{5/2}} && w_{3,3} = \frac{-451+131c+815c^2+105c^3}{768R^5\sqrt{2}(1-c)^{7/2}} \\ &w_{1,4} = \frac{-85+70c+315c^2}{256R^4\sqrt{2}(1-c)^{5/2}} && w_{3,4} = \frac{1315-8075c-9695c^2-945c^3}{6144R^6\sqrt{2}(1-c)^{7/2}} \\ &w_{2,0} = \frac{1-3c}{8R\sqrt{2}(1-c)^{3/2}} && w_{4,0} = \frac{7+6c-c^2}{256R^3\sqrt{2}(1-c)^{5/2}} \\ &w_{2,1} = \frac{5+9c}{16R^2\sqrt{2}(1-c)^{3/2}} && w_{4,1} = \frac{-61-26c+3c^2}{256R^4\sqrt{2}(1-c)^{5/2}} \\ &w_{2,2} = \frac{-27+18c+45c^2}{64R^3\sqrt{2}(1-c)^{5/2}} && w_{4,2} = \frac{75-507c-183c^2+15c^3}{1024R^5\sqrt{2}(1-c)^{7/2}} \\ &w_{2,3} = \frac{7-130c-105c^2}{128R^4\sqrt{2}(1-c)^{5/2}} && w_{4,3} = \frac{1065+2255c+515c^2-35c^3}{2048R^6\sqrt{2}(1-c)^{7/2}} \\ &w_{2,4} = \frac{395+965c-1015c^2-945c^3}{1024R^5\sqrt{2}(1-c)^{7/2}} && w_{4,4} = \frac{-14595+1500c+27270c^2+5740c^3-315c^4}{16384R^7\sqrt{2}(1-c)^{9/2}} \end{aligned} \quad (16) $$

where $c = \cos\psi$.

Martinec et al. (1996) have already proven that a series expansion of gravitational potential or attraction is divergent if the integration [such as in Eq. (15)] is entirely global. However, if one restricts the integration to an 'outer zone' outside a cap of radius $\psi = \psi_c$, then this series will be seen to be convergent. To whit, the $w_{i,j}$ kernels must be set to zero inside a cap radius, ψ_c

$$ w_{i,j} = \begin{cases} w_{i,j} & \psi > \psi_c \\ 0 & \psi \le \psi_c \end{cases} \quad (17) $$

The convergence of this series will be shown empirically in a later section.

4.2 Gravitational attraction of 2-D masses on the geoid computed at the Earth's surface ($_C g_P$)

In the R/r/D path of the Stokes–Helmert scheme, the attraction due to the condensed topography must be known at the Earth's surface (point P). As before, begin with gravitational potential, but induced by a 2-D condensed topographic mass layer (C) on the geoid (spherical surface $r = R$)

$$ {}_C W_P = {}_C W(r_P, \phi_P, \lambda_P) = \int_A \frac{G}{l} \kappa \, \mathrm{d}A \quad (18) $$

where integration is now over an area 'A' and not a volume 'V', and $\kappa \, \mathrm{d}A$ is the differential mass element (surficial density times differential area element). Expanding

$$ {}_C W_P = \int_{\varphi} \int_{\lambda} \frac{G\kappa}{l} \mathrm{d}A = \int_{\varphi} \int_{\lambda} \frac{G\kappa}{l} R^2 \cos\varphi \, \mathrm{d}\lambda \, \mathrm{d}\varphi \quad (19) $$

Note that the surficial density layer has the following *exact* (in spherical coordinates, using a purely vertical, non-lateral, condensation method) density formula (Smith et al. 2001):

$$ \kappa(\varphi,\lambda) = \rho H_*(\varphi,\lambda) = \rho\left[H + \frac{H^2}{R} + \frac{H^3}{3R^2}\right] \quad (20) $$

and that the distance function is now [compare to Eq. (5)]

$$ l = \sqrt{R^2 + r_P^2 - 2Rr_P\cos\psi} \quad (21) $$

To obtain the gravitational attraction, the radial derivative is taken as per Eq. (7), yielding

$$ {}_C g_P = \int_{\varphi} \int_{\lambda} \frac{G\rho H_* R^2 (R\cos\psi - r_P)}{\left[\sqrt{R^2 + r_P^2 - 2Rr_P\cos\psi}\right]^3} \cos\varphi \, \mathrm{d}\lambda \, \mathrm{d}\varphi \quad (22) $$

with $r_P = R + H_P$, and H_* from Eq. (20). Similarly to Eq. (9), it is necessary to separate the H_*, H_P and ψ variables in Eq. (22). However, since H_* and ψ are separated from one another already, a series expansion in H_P is all that is necessary. Performing that expansion

and applying it to Eq. (22) yields the following sum of integrals:

$$ {}_{C}g_P = G\rho \sum_{j=0}^{\infty} H_P^j \int_{\varphi} \int_{\lambda} H_* v_j \cos\varphi \, \mathrm{d}\lambda \, \mathrm{d}\varphi \tag{23} $$

where the v_j kernels (to $j = 4$) are as follows:

$$ \begin{aligned} v_0 &= \frac{1}{2\sqrt{2}(1-c)^{1/2}} \\ v_1 &= -\frac{1-3c}{4R\sqrt{2}(1-c)^{3/2}} \\ v_2 &= \frac{-3-15c}{16R^2\sqrt{2}(1-c)^{3/2}} \\ v_3 &= \frac{13+10c-35c^2}{32R^3\sqrt{2}(1-c)^{5/2}} \\ v_4 &= \frac{-85+70c+315c^2}{256R^4\sqrt{2}(1-c)^{5/2}} \end{aligned} \tag{24} $$

where, again, $c = \cos\psi$. It is interesting to note the close similarity between the v_j kernels and the $w_{1,j}$ kernels of Sect. 4.1, even though the variable used here is H_* while that in 4.1 was H. In order to enforce a convergence of the series, it is necessary to force the v_j kernels to follow this rule

$$ v_j = \begin{cases} v_j & \psi > \psi_c \\ 0 & \psi \le \psi_c \end{cases} \tag{25} $$

4.3 Gravitational attraction of 2-D masses on the geoid computed at the geoid $({}_{C}g_{P_0})$

If one pursues the R/D/r path of the Stokes–Helmert scheme, then the computational point for the 2-D mass attraction is at the geoid ($r_P = R$). As shown in Smith et al. (2000), the gravitational attraction of interest is not actually on the geoid itself but is the limiting value of attraction as r_P approaches R from outside the geoid. In more well known calculus usage, $(r_P - R)$ approaches 0 from the positive side.

$$ {}_{C}g_{P_0} = \lim_{(r_P - R) \to 0+} {}_{C}g_P \tag{26} $$

Applying this limit to Eq. (23) yields

$$ {}_{C}g_{P_0} = G\rho \int_{\varphi} \int_{\lambda} (H_* \cos\varphi) \frac{1}{2\sqrt{2}(1-c)^{1/2}} \, \mathrm{d}\lambda \, \mathrm{d}\varphi \tag{27} $$

where, again, c is $\cos\psi$. Note that this equation has been arranged to emphasize the fact that a convolution exists without the need for expansion into a series. This is one definite advantage to the R/D/r approach. The kernel, u, in Eq. (27) above is

$$ u = \frac{1}{2\sqrt{2}(1-c)^{1/2}} \tag{28} $$

and using it to compute outer-zone effects, it follows that

$$ u = \begin{cases} u & \psi > \psi_c \\ 0 & \psi \le \psi_c \end{cases} \tag{29} $$

4.4 Gravitational potential of 3-D masses computed at the geoid $({}_{T}W_{P_0})$

Without regard for the path chosen in the Stokes–Helmert approach, the indirect effect on geoid undulations is computed the same way – through determination of potential change on the geoid due to Helmertization of the topography (Heiskanen and Moritz 1967; Wichencharoen 1982; Sjöberg and Nahavandchi 1999). This potential change is computed in two parts: the removal of 3-D masses causes one shift in the potential field, and then the restoration of the 2-D masses causes the second shift. The combined displacement of the geoid due to these two shifts is the indirect effect. This section discusses the shift in potential at the geoid due to the removal of topography. Section 4.5 will discuss the potential shift at the geoid due to restoring the condensed topography.

The gravitational potential at the geoid ($r_P = R$) induced by the 3-D topography is

$$ {}_{T}W_{P_0} = {}_{T}W(R, \phi_P, \lambda_P) = \int_{V} \frac{G}{l} \rho \, \mathrm{d}V \tag{30} $$

where G is the Universal gravitational constant, V is the volume of the 3-D topography, $\rho \, \mathrm{d}V$ is a differential mass element (density times differential volume element), and l is the distance between P_0 and $\rho \, \mathrm{d}V$. Note that $\phi_P = \phi_{P_0}$ and $\lambda_P = \lambda_{P_0}$ due to the vertical alignment of points P and P_0. This equation can be expanded more formally as

$$ {}_{T}W_{P_0} = \int_{\varphi} \int_{\lambda} \int_{r} \frac{G\rho}{l} \, \mathrm{d}V = \int_{\varphi} \int_{\lambda} \int_{r} \frac{G\rho}{l} r^2 \cos\varphi \, \mathrm{d}r \, \mathrm{d}\lambda \, \mathrm{d}\varphi \tag{31} $$

where the distance l can now be written as [contrast with Eqs. (5) and (21)]

$$ l = \sqrt{r^2 + R^2 - 2rR\cos\psi} \tag{32} $$

The integral in r may be removed analytically from Eq. (31), leaving

$$ \begin{aligned} {}_{T}W_{P_0} = \int_{\varphi} \int_{\lambda} G\rho \Bigg[& \frac{1}{2}(r - 3R\cos\psi)\sqrt{r^2 + R^2 - 2rR\cos\psi} \\ & - \frac{1}{2}(R^2 - 3R^2\cos^2\psi) \\ & \times \ln\left(r - R\cos\psi + \sqrt{r^2 + R^2 - 2rR\cos\psi}\right) \Bigg]_{r=r_1(\varphi,\lambda)}^{r=r_2(\varphi,\lambda)} \\ & \times \cos\varphi \, \mathrm{d}\lambda \, \mathrm{d}\varphi \end{aligned} \tag{33} $$

where $r_2 = R + H$ and $r_1 = R$. Once again it is desirable to separate H from ψ (there is no H_P dependence since the computation point is on the geoid where $r_P = R$, or $H_P = 0$) in Eq. (33). This is done through a series in H. Performing the expansion and substituting it into Eq. (33) yields

$$ {}_T W_{P_0} = G\rho \sum_{i=0}^{\infty} \int_{\varphi} \int_{\lambda} H^i x_i \cos\varphi \, \mathrm{d}\lambda \, \mathrm{d}\varphi \tag{34} $$

with the kernels x_i taking the following values (up to $i = 4$):

$$ \begin{aligned} x_0 &= 0 \\ x_1 &= \frac{R}{\sqrt{2}(1-c)^{1/2}} \\ x_2 &= \frac{3}{4\sqrt{2}(1-c)^{1/2}} \\ x_3 &= \frac{1-3c}{24\sqrt{2}R(1-c)^{3/2}} \\ x_4 &= \frac{3-4c+c^2}{64\sqrt{2}R^2(1-c)^{3/2}} \end{aligned} \tag{35} $$

where $c = \cos\psi$. Once again, to allow a convergence in the series, the kernels are modified to work in the outer zone only.

$$ x_i = \begin{cases} x_i & \psi > \psi_c \\ 0 & \psi \le \psi_c \end{cases} \tag{36} $$

4.5 Gravitational potential of 2-D masses on the geoid computed at the geoid ($_C W_{P_0}$)

In a similar manner as Sect. 4.3, limits are used to determine the gravitational potential induced by condensed masses on the geoid for a point 'on' the geoid

$$ {}_C W_{P_0} = \lim_{(r_P - R) \to 0+} {}_C W_P \tag{37} $$

where $_C W_P$ is found in Eq. (19). Applying this limit yields

$$ {}_C W_{P_0} = G\rho \int_{\varphi} \int_{\lambda} (H_* \cos\varphi) \frac{R}{\sqrt{2}(1-c)^{1/2}} \, \mathrm{d}\lambda \, \mathrm{d}\varphi \tag{38} $$

where $c = \cos\psi$. Eq. (38) was arranged to emphasize the fact that a convolution exists without the need for a series expansion. The kernel, y, in Eq. (38) is therefore

$$ y = \frac{R}{\sqrt{2}(1-c)^{1/2}} \tag{39} $$

and like all other kernels thus far, it is used only in the outer zone

$$ y = \begin{cases} y & \psi > \psi_c \\ 0 & \psi \le \psi_c \end{cases} \tag{40} $$

5 Numerical tests

5.1 Shell tests

Before proceeding with real DEM data, the new formulae were tested in a simple shell test. A global, spherical shell 1000 m high was built on a 1×1 degree grid, referenced to the centers of the 1×1 degree cells, surrounding a reference sphere of radius 6 371 000 m. Because such a 'shell' has known analytical properties, it was possible to compare the results from the 1-D FFT formulae to true values. Using Eq. (2) applied to each integral of Eq. (15), a 1-D FFT solution to this shell was computed (to $i, j = 4$) for an outer zone defined by a cap of radius $\psi_c = 4$ degrees. A cut-off radius of 4 degrees was chosen primarily to be consistent with the results found in Smith et al. (2001). Other radii can be chosen, but if ψ_c is too small, then Gibbs' phenomena associated with the discontinuous kernels at ψ_c near the station of interest may cause errors. If ψ_c is too large, then the computational burden on the inner zone becomes excessively large.

In analytical form the gravitational attraction computed at the surface of the Earth for a shell H m thick, outside a cap of radius ψ_c, is (derived through Mathematica 4.0 software)

$$ \begin{aligned} &{}_T g_P \ (H = \text{const}; \psi \ge \psi_c) \\ &= \frac{2\pi G\rho}{3} \left\{ \begin{array}{l} \left[\frac{1}{d^2}\left(d^3 - R^3 + l\left(l^2 + 3c^2d^2 - 3d^2 - cdR\right)\right)\right] \\ +\left[(1 - c - 3c^2)d\sqrt{2-2c} + (3c^3 d - 3cd)\right. \\ \left.\left(\ln\left[R - cd + l\right] - \ln\left[d - cd + d\sqrt{2-2c}\right]\right)\right] \end{array} \right\} \end{aligned} \tag{41} $$

where

$$ \begin{aligned} d &= R + H \\ c &= \cos\psi_c \\ l &= \sqrt{d^2 - 2cdR + R^2} \end{aligned} $$

For this test, the thickness of the shell is 1000 m, the cap ψ_c is 4 degrees, and the following constants are used

$$ \begin{aligned} G &= 6672.6 \times 10^{-14}\,\mathrm{m^3\,s^{-2}\,kg^{-1}} \\ \rho &= 2.67 \times 10^3\,\mathrm{kg\,m^{-3}} \\ R &= 6\,371\,000\,\mathrm{m} \end{aligned} $$

With these values, the attraction $_T g_P$ for the shell is 108.142 mGal, everywhere. Using a 1×1 degree DEM and Eq. (15), the output values differed slightly from this value. They are listed in Table 1. While Table 1 indicates a near match to the analytical solution, it was

Table 1. Statistics of T_{gP} for initial 1000-m shell test (mGal)

	Analytical	1-D FFT with 1×1 arcdegree DEM	Difference
Average	108.142	108.680	−0.538
Standard deviation	±0.000	±0.232	0.232
RMS	108.142	108.680	−0.538
Minimum	108.142	108.167	−0.025
Maximum	108.142	108.995	−0.853

at first discouraging to see that any disagreement existed. In order to get a graphical idea of where the deviations are arising, a south pole to north pole slice of the FFT solution is provided in Fig. 4. This figure shows two primary deviations from the (expected) flat line at 108.142 mGal. The first is a generally parabolic deviation, being worst at the equator. The second deviation is high-frequency deviations along that parabolic mismatch.

A reason for the 2nd (high-frequency) issue was hypothesized: the kernels were being computed from one grid point to another, with strict adherence to Eqs. (16) and (17). However, if one interprets a grid point as the center of a cell, then this means a 'cell' might lie partially outside the cap while the center of the cell lies inside the cap, or vice versa. A 'cell' which lies partly inside and partly outside the cap, but which was either being given full weight ($\psi > \psi_c$) or no weight ($\psi < \psi_c$) was not being properly accounted for. To test this hypothesis, an examination of the method of computing kernels, w_{ij}, was made and is described below.

5.1.1 Test of weighting for near-cap-radius kernels

In the first FFT run, the distance, ψ, was computed between point P and the center of a cell, and the rule in Eq. (17) rigorously applied. That is, the kernel followed the following rule:

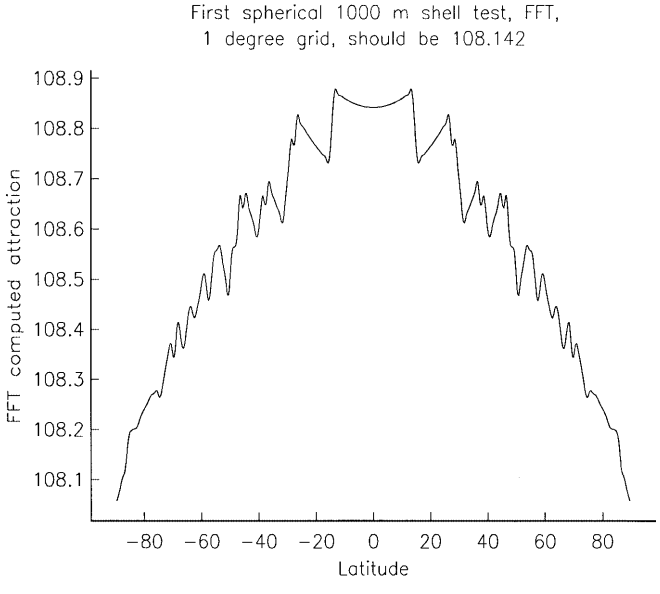

Fig. 4. First spherical shell test results on a 1-degree shell DEM, showing pole-to-pole values at every 1 degree

$$w_{i,j} = \begin{cases} w_{i,j} & \psi_0 > \psi_c \\ 0 & \psi_0 \le \psi_c \end{cases} \tag{42}$$

where ψ_0 is the spherical distance from one grid node to another (or from the center of one cell to another). The problem turns out that some cells might just barely have their centers outside the cap, and thus be fully weighted, while neighboring cells might have their centers just barely inside the cap and given zero weight. See Fig. 5 for elucidation of this issue. This is very similar to the 'line mass vs prism mass' issue discussed in Li and Sideris (1994). This issue also neatly exemplifies the problem of using a circular cap with a regular DEM grid. In an attempt to correct this issue, a scaling rule for the kernel functions was investigated. That is, a variation on Eq. (42) was proposed

$$w_{i,j} = \begin{cases} w_{i,j}(\psi_0) & \psi > \psi_c \forall \psi \text{ (in a cell)} \\ s \cdot w_{i,j}(\psi_0) & \psi > \psi_c \text{ for some, not all, } \psi \text{ (in a cell)} \\ 0 & \psi \le \psi_c \forall \psi \text{ (in a cell)} \end{cases} \tag{43}$$

where ψ is now computed from P to *all points* over a cell, not just the center point, but the final kernel is still based on $\psi = \psi_0$, where ψ_0 is the distance from P to the *center* of a cell. The rule for determining s in Eq. (43) is not easy to deduce. It is dependent on the size of the cell, the size of ψ_c, the latitude of P, the azimuth from P to the cell, the height of P, the height of the cell and the percent of the cell that lies outside the cap! However, some simple empirical tests indicate that the following rule is generally adhered to, in spite of all these variables (for our case of $\psi_c = 4$ degrees), when the heights are in the range of real heights on Earth:

$$s = k \cdot A_o \tag{44}$$

where A_o represents the fraction of the cell that lies outside the cap (and is therefore a number between 0 and 1) relative to point P, and k takes on values ranging from 1.0 to 1.17. Figure 6 shows a few examples of A_o values near the cap edge. As a first attempt to remove the 'high-frequency' problem in the spherical shell test, Eq. (44) was applied to Eq. (43) and fixing $k = 1.0$. The

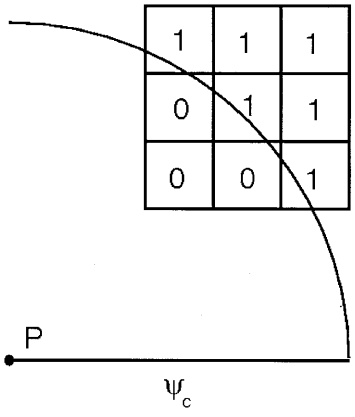

Fig. 5. Initial weighting scheme for cells near the cap edge

statistics of that run are found in Table 2. While those values still show a large deviation from the constant 108.142 mGal, the real story is in the cross section of this test, shown in Fig. 7. Here it is clearly seen that the scaling of weight functions for cells 'on the edge' of the cap radius was clearly the solution to the high-frequency deviations seen previously. Thus the hypothesis regarding high-frequency deviations was proved true.

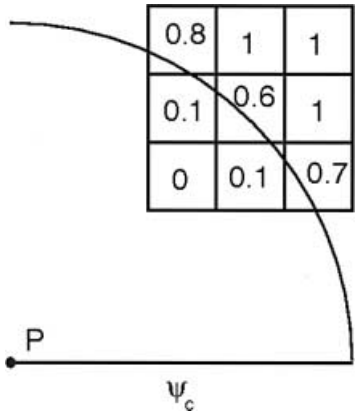

Fig. 6. Value of A_0 near the cap edge (also the same as the values of the scale factor s for the kernel if the weight $k = 1.0$)

Table 2. Statistics of $_{TgP}$ for 2nd 1000-m shell test (mGal)

	Analytical	1-D FFT with 1×1 degree DEM and 'partial cell' weighting near $\psi = \psi_c$	Difference
Average	108.142	108.563	−0.421
Standard deviation	±0.000	±0.200	0.016
RMS	108.142	108.563	−0.421
Minimum	108.142	108.149	0.007
Maximum	108.142	108.802	−0.660

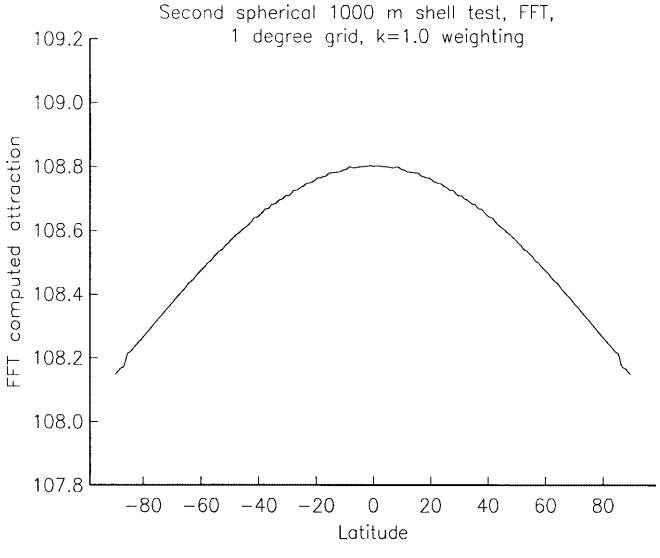

Fig. 7. Second spherical shell test results scaling by $s = kA_0$ with a weight $k = 1.0$ for each kernel and a 1-degree shell DEM, showing pole-to-pole values at every 1 degree

5.1.2 Parabolic deviation

The cause for the parabolic bias in Fig. 4 was investigated next. Bugs in the code were ruled out first, meaning some theoretical issue had been left unsolved. It was believed that a secondary effect of the 'line mass vs. prism mass' (Li and Sideris 1994) argument was being seen. Specifically, the difference between the kernel computed for ψ_0 of any given cell and the average kernel over that cell was suspected. That is, a link was hypothesized between the latitude dependence of Fig. 4 and the following difference:

$$\Delta w_{i,j} = w_{i,j}(\psi_0) - \overline{w_{i,j}} \tag{45}$$

where

$$w_{i,j}(\psi_0) = w_{i,j}(\psi[\phi_0, \phi_P, \lambda_0 - \lambda_P]) \tag{46}$$

and

$$\overline{w_{i,j}} = \int_{\phi=\phi_1}^{\phi_2} \int_{\lambda=\lambda_1}^{\lambda_2} w_{i,j}(\psi[\phi, \phi_P, \lambda - \lambda_P]) \mathrm{d}\lambda \, \mathrm{d}\phi \tag{47}$$

and

$$\begin{aligned} \phi_0 &= \frac{\phi_1 + \phi_2}{2} \\ \lambda_0 &= \frac{\lambda_1 + \lambda_2}{2} \end{aligned} \tag{48}$$

Unfortunately, Eq. (45) has no known analytical solution, making a link between $\Delta w_{i,j}$ and the parabola in Fig. 4 possible only through an empirical study. While such a study is possible, it has been postponed for a future paper, in favor of a faster solution: smaller DEM spacing. According to Li and Sideris (1994), a smaller grid spacing can reduce the line mass vs point mass issue. As such, a new 'shell' test was performed, this time using a 5-arcminute grid, rather than a 1-degree grid, and using the weighting scheme ($s = k \cdot A_0$, with $k = 1.0$) described above for the reduction of high-frequency errors. The statistical results of those results are presented in Table 3 and a 'slice' of the output from south pole to north pole, at any given longitude, is presented in Fig. 8. Comparing Fig. 7 to Fig. 8, one can

Table 3. Statistics of $_{TgP}$ for 3rd 1000-m shell test (mGal)

	Analytical	1-D FFT with 5×5 arcminute DEM and 'partial cell' weighting near $\psi = \psi_c$	Difference
Average	108.142	108.176	−0.034
Standard deviation	±0.000	±0.016	0.016
RMS	108.142	108.176	−0.034
Minimum	108.142	108.142	0.000
Maximum	108.142	108.196	−0.054

see that the pole-to-equator parabolic deviation has been reduced from 0.653 to 0.054 mGal. At this time, 0.054 mGal is considered within an acceptable error budget, even though such an effect can impact the geoid at the 2–3-cm level. This is because the nature of this test is a global shell, which is different than the true Earth topography (predominantly zero elevation), and as such we expect an even smaller impact when the final computations are made using true Earth topography models. (The reason differences exist at all seems to stem from the prism mass vs line mass issue. In the future, a more rigorous 'prism mass' formulation of this problem should yield closer agreement with the numerical integration results.) As such, a scale factor of $k = 1.0$ in accordance with Eq. (44), and a 5-arcminute grid, were assumed acceptable criteria for applying this 1-D FFT method. As an actual data test, the next section discusses the use of a real DEM.

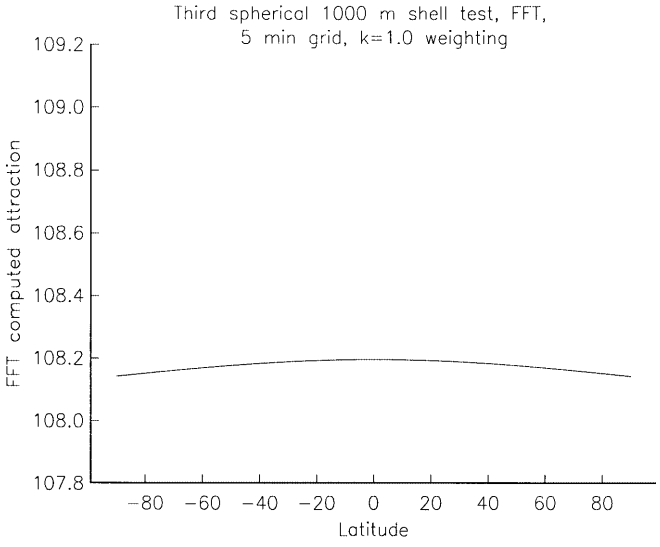

Fig. 8. Third spherical shell test results scaling by $s = kA_0$ with a weight $k = 1.0$ for each kernel and a 5-arcminute shell DEM, showing pole-to-pole values at every 1 degree

Table 4. Statistics of $_{T}g_{P}$ for global 1-D FFT using GLOBE_5min (mGal)

Average	26.649
Standard deviation	±6.231
RMS	27.368
Minimum	17.441
Maximum	50.056

5.2 DEM tests

The 1-D FFT approach was applied to the $_{T}g_{P}$ in Eq. (15), using the scaling mentioned in Sect. 5.1.1, and a 5-arcminute grid (called GLOBE_5min), averaged from the 30-arcsecond GLOBE 1.0 grid (Hastings and Dunbar 1999), which will be called GLOBE_30sec. The statistics of $_{T}g_{P}$ for all 5-arcminute grid points globally is stated in Table 4, and shown in shaded contour in Fig. 9.

In order to test the success of the 1-D FFT method, it was tested at a few locations using a quadrature method. Due to the length of time needed for quadrature, it was impossible to test all points against the 1-D FFT method, so a few smaller tests were devised. As a first test, at a series of points running from south pole to north pole $_{T}g_{P}$ was computed using quadrature. These points ranged from $-89°30'$ to $+89°30'$, at every 1 degree (180 points). The statistical differences between the quadrature-based $_{T}g_{P}$ at these points and that from the 1-D FFT method are listed in Table 5. A graph of these differences is plotted in Fig. 10. Statistically, the deviations between quadrature and FFT along this meridian are small, relative to errors in data collection, theory, and knowledge of rock density, and are therefore con-

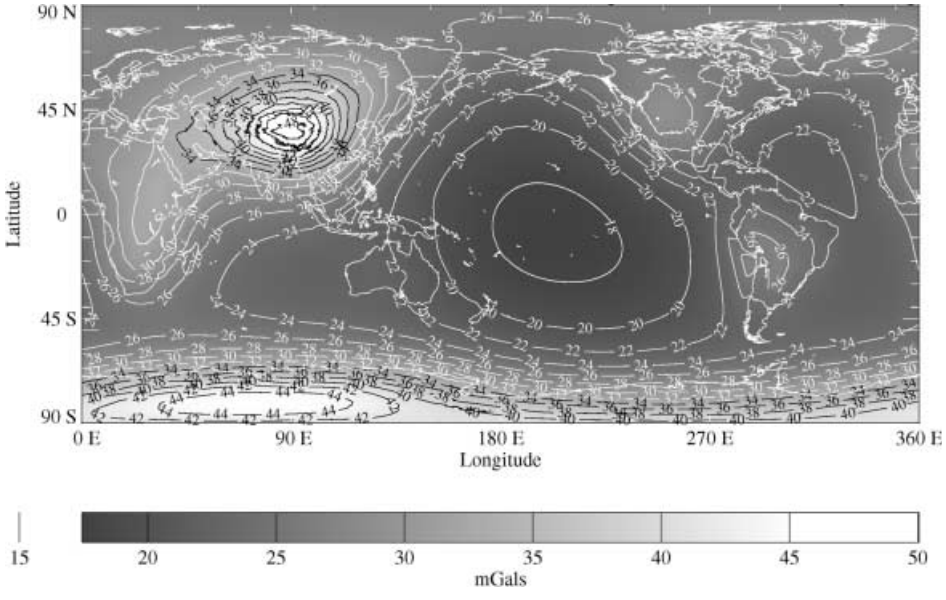

Fig. 9. Gravitational attraction, computed at the Earth's surface, of 3-D topographic masses, outside a 4-degree cap, using 1-D FFT, GLOBE_5min DEM and $k = 1.0$ weighting

sidered acceptable. It is interesting to note, however, that the largest deviations from zero are correlated with shorelines (the largest spike in Fig. 10 of 0.11 mGal occurs at the shoreline of Antarctica). It may be that the sharp breaks between topographic elevations and oceanic zero elevations that occur at shorelines are difficult to model with a Fourier series and therefore cause the largest errors in this method. Nonetheless, even the largest errors are small and localized and for current purposes are considered acceptable.

A second test was merely to take 10 points around the globe, all in highly mountainous topography, and test quadrature versus 1-D FFT at those points. Their locations are given in Table 6, as well as the statistical differences of quadrature versus 1-D FFT at those points. With the largest error being only −0.041 mGal at Mt. Everest, no significant error is expected due to extraordinarily high topography. These two tests show that some small, but acceptable, numerical errors can exist in the 1-D FFT method (using the 'line mass' method), making it a useful alternative to quadrature.

Table 5. Statistics of ${}_{T}g_{P}$ for initial pole-to-pole ($l = 20.5°$, $-89.5° \le f \le +89.5°$) test using GLOBE_5min (mGal)

	Quadrature	1-D FFT	Difference
Average	30.284	30.288	−0.005
Standard deviation	±4.266	±4.268	±0.020
RMS	30.581	30.586	0.020
Minimum	25.073	25.074	−0.030
Maximum	43.065	43.071	0.111

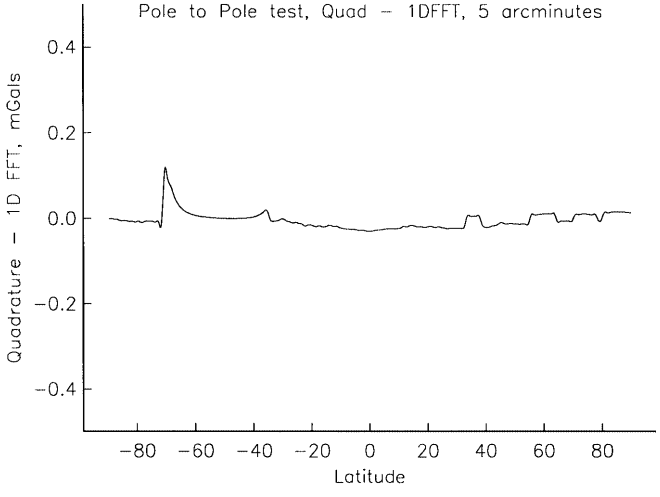

Fig. 10. Pole-to-pole test ($l = 20.5$ degrees) of quadrature versus 1-D FFT at 1-degree increments

6 Global computations

Having been satisfied that the global ${}_{T}g_{P}$ computations are working properly, a global set of ${}_{C}g_{P}$, ${}_{C}g_{P_0}$, ${}_{T}W_{P_0}$ and ${}_{C}W_{P_0}$ were performed using Eqs. (23), (27), (34), and (38), using the kernel weighting scheme $s = k \cdot A_0$, with $k = 1.0$. The results, and computation times, are shown in Table 7, and plotted in Figs. 11–14. Additionally, statistics of each component of the series expansions used (for ${}_{T}g_{P}$, ${}_{C}g_{P}$, and ${}_{T}W_{P_0}$) are given in Tables 8, 9 and 10, and in each of these tables one can clearly see that the expansion to degree 4 was sufficient in all cases. Few details are obvious in these global plots. One thing that is obvious is the close relation between ${}_{C}g_{P}$ and ${}_{C}g_{P_0}$ (Figs. 11 and 12), indicating that one must be careful which value is used. The plots look similar, but are, in fact, slightly different in systematic ways that will impact the final geoid computation if the wrong gravity reduction is used. Also, because ${}_{T}g_{P}$ and ${}_{C}g_{P}$ (Figs. 9 and 11) are each dependent on powers of H_P, there is significant detail due to the high correlation between those two quantities and the topography itself. This issue is covered extensively in Sect. 7.

Table 7. Statistics for ${}_{C}g_{P}$, ${}_{C}g_{P_0}$, ${}_{T}W_{P_0}$ and ${}_{C}W_{P_0}$ for global 1-D FFT using GLOBE_5min (mGal for g values and $m^2\ s^{-2}$ for W values)

	${}_{C}g_{P}$	${}_{C}g_{P_0}$	${}_{T}W_{P_0}$	${}_{C}W_{P_0}$
Average	26.750	26.636	3393.648	3393.916
Standard deviation	±6.382	±6.132	±781.277	±781.362
RMS	27.501	27.332	3482.418	3482.699
Minimum	17.445	17.445	2222.61	2222.78
Maximum	51.172	48.468	6175.17	6175.84
Computation time (h)	∼45	∼9	∼36	∼9

Table 6. ${}_{T}g_{P}$ test, quadrature versus 1-D FFT, at 10 mountainous points across the globe

Location information				Results (mGal)		
Latitude	Longitude	Height	Description	Quadrature	1-D FFT	Difference
45.5	245.5	2144	Rocky Mts	28.948	28.956	−0.008
58.5	235.5	1604	Rocky Mts	26.965	26.977	−0.012
53.5	240.5	2226	Rocky Mts	27.614	27.623	−0.009
58.5	234.5	2129	Rocky Mts	26.845	26.857	−0.012
62.5	232.5	1473	Rocky Mts	26.547	26.555	−0.008
35.5	77.5	5502	Everest	45.532	45.573	−0.041
−0.5	36.5	2510	Kilimanjaro	32.223	32.232	−0.009
−89.5	20.5	2794	Antarctica	41.258	41.258	0.000
−18.5	293.5	3821	Andes	26.135	26.141	−0.006
70.5	320.5	3056	Greenland	27.376	27.373	+0.003

7 Practical application for high-resolution DEMs

The previous sections dealt with globally computing gravity field components on grid points, where the grid points are identical to the DEM grid points themselves (i.e. a 5-arcminute gridded global DEM yielded gravitational values on a 5-arcminute output grid). However, it is often necessary in geoid modeling to have topographic effects computed on a much finer grid than 5-arcminutes. On the other hand, a global 1-arcsecond DEM is not available, and even if it were the computational time to work with this method would be months, at best. There is a solution, however. Note that Eq. (15) can be written as the (scaled) sum of products of two values, H_P^j and ${}_wQ_j$, which exist at any given point P.

$$
\begin{aligned}
{}_Tg_P &= G\rho \sum_{j=0}^{\infty} H_P^j \sum_{i=0}^{\infty} \int_{\varphi} \int_{\lambda} H^i w_{i,j} \cos\varphi \, \mathrm{d}\lambda \, \mathrm{d}\varphi \\
&= G\rho \sum_{j=0}^{\infty} H_P^j(\phi_P, \lambda_P)\, {}_wQ_j(\phi_P, \lambda_P)
\end{aligned} \tag{49}
$$

where the ${}_wQ_j$ term is obvious by implication. Thankfully, the ${}_wQ_j$ term is computed as a next-to-final step in computing ${}_Tg_P$ in the software, so capturing it as a separate by-product grid causes no additional computational burden. In a straightforward application of

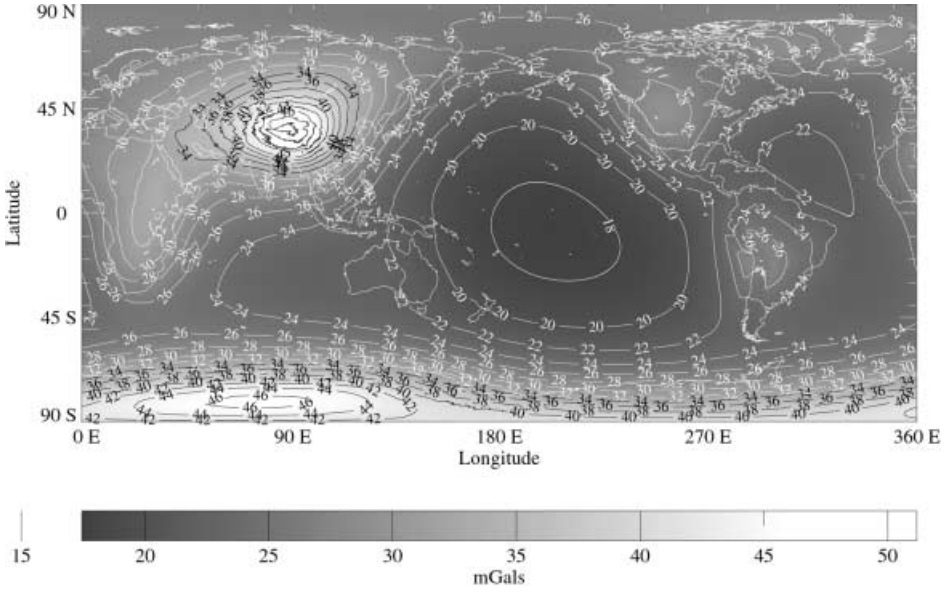

Fig. 11. Gravitational attraction, computed at the Earth's surface, of 2-D topographic masses, outside a 4-degree cap, using 1-D FFT, GLOBE_5min DEM and $k = 1.0$ weighting

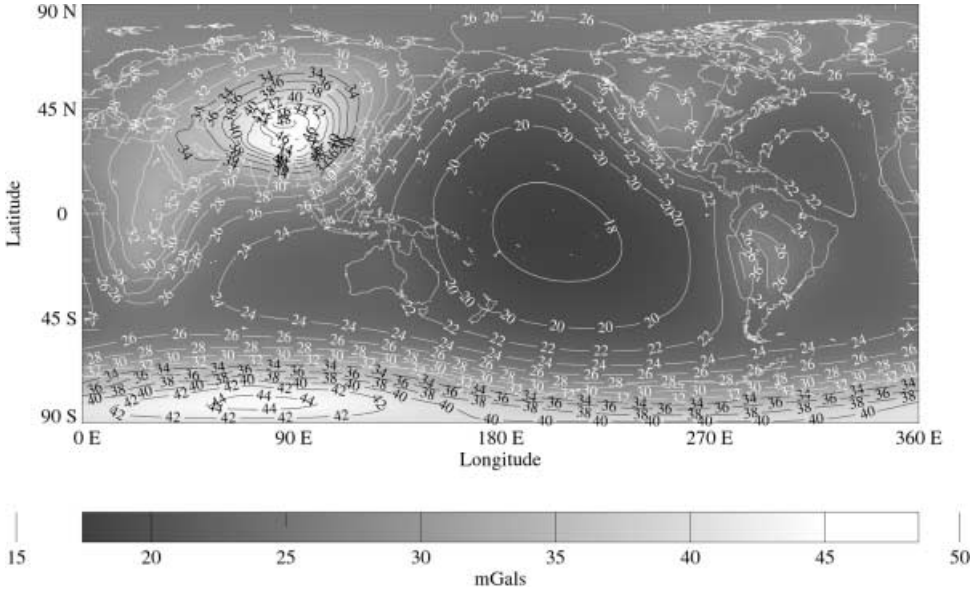

Fig. 12. Gravitational attraction, computed at the geoid, of 2-D topographic masses, outside a 4-degree cap, using 1-D FFT, GLOBE_5min DEM and $k = 1.0$ weighting

Eq. (15), the DEM grid spacing is equivalent to the ${}_wQ_j$ and H_P^j, and thus the ${}_Tg_P$ spacing. However, ${}_wQ_j$ is a very long wavelength signal, while H_P^j is a localized short-wavelength signal (and convolving ${}_wQ_j$ with H_P^j therefore yields a ${}_Tg_P$ grid that has both long and short wavelength features). As such, one can compute ${}_wQ_j$ at 5 arcminutes, for example, but accurately interpolate between those grid nodes to a finer grid, say 1 arcsecond, with confidence. As such, a fine grid (1 arcsecond) of heights (H_P), consistent with the 5-arcminute DEM, can be used with a 'densified' ${}_wQ_j$ grid (computed at 5 arcminutes, interpolated down to 1 arcsecond), and Eq. (49) applied. In this way, the high-frequency H_P information is successfully, and accurately, merged with the long-wavelength ${}_wQ_j$ information, yielding the correct values for ${}_Tg_P$ on a grid of 1 arcsecond, without needing a global 1-arcsecond DEM. Of course, this method can also be applied to ${}_Cg_P$ as well, but with Eq. (23) being modified

$$
\begin{aligned}
{}_Cg_P &= G\rho \sum_{j=0}^{\infty} H_P^j \int_{\varphi} \int_{\lambda} H_* v_j \cos\varphi \, \mathrm{d}\lambda \mathrm{d}\varphi \\
&= G\rho \sum_{j=0}^{\infty} H_P^j(\phi_P, \lambda_P)\, {}_vQ_j(\phi_P, \lambda_P)
\end{aligned}
\tag{50}
$$

It should be further noted that this ability to break the computations down into a long-wavelength 'Q' component, easily convolved with a high-resolution DEM unique to this (FFT) approach, and is not found in papers where global effects are computed using spherical harmonics (Nahavandchi 2000; Sjöberg 2000).

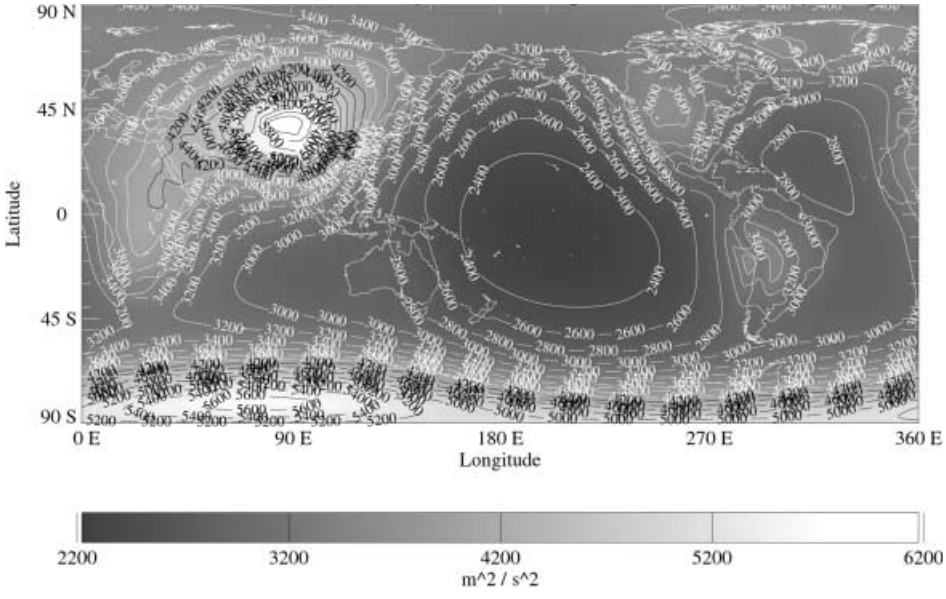

Fig. 13. Gravitational potential, computed at the geoid, of 3-D topographic masses, outside a 4-degree cap, using 1-D FFT, GLOBE_5min DEM and $k = 1.0$ weighting

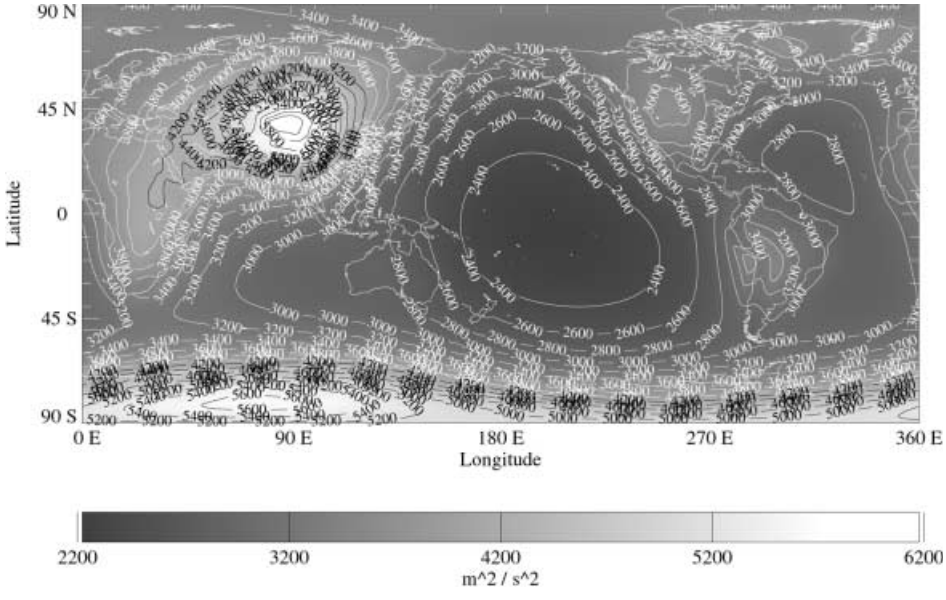

Fig. 14. Gravitational potential, computed at the geoid, of 2-D topographic masses, outside a 4-degree cap, using 1-D FFT, GLOBE_5min DEM and $k = 1.0$ weighting

This method of breaking the computation into long-wavelength (${}_vQ_j$ or ${}_wQ_j$) and short-wavelength (H_P^j) components is unnecessary for the values ${}_Cg_{P_0}$, ${}_TW_{P_0}$, and ${}_CW_{P_0}$, as they all have no dependence on an H_P term.

This method for computing both ${}_Tg_P$ and ${}_Cg_P$ was applied in a mountainous 1×1 degree region ($39° \le f \le 40°$, $254° \le l \le 255°$) of the western United States using the 1-arcsecond DEM NGSDEM99 (Smith and Roman 2001b). The rugged topography of that region is shown in Fig. 15. The ${}_vQ_j$ and ${}_wQ_j$ components were first computed separately from the global 5-arcminute DEM, and then interpolated to 1 arcsecond using bicubic splines. They were then convolved with the 1-arcsecond H_P^j grids based on NGSDEM99. Some interesting results were found and are discussed below.

7.1 High-resolution results

The statistics for the final computations of ${}_Tg_P$ and ${}_Cg_P$ at 1 arcsecond are found in Table 11 and the corresponding results based solely on the 5-arcminute DEM (interpolated down to 1 arcsecond) are also in that table. A plot of the true 1-arcsecond ${}_Tg_P$ values is shown in Fig. 16 while its counterpart (5-arcminute interpolated down to 1 arcsecond) is plotted in Fig. 17. Note the significant gain in detailed gravity field knowledge for Fig. 16 over Fig. 17. Similar (so similar that showing them is unnecessary) plots can be made of ${}_Cg_P$.

What impact these high-resolution values of ${}_Tg_P$ and ${}_Cg_P$ have on the geoid can only be answered by knowing which path one is taking toward Helmert space – R/r/D or R/D/r. This is discussed in Sect. 7.2.

7.2 High-resolution results and the path toward Helmert space

Are high-resolution values of ${}_Tg_P$ and ${}_Cg_P$ needed for computing an accurate model of the geoid? The answer is: It depends on your path toward Helmert space. Remember that in the R/r/D path, a topographic reduction of '$-{}_Tg_P + {}_Cg_P$' is made to surface gravity. And while, individually, the 1-arcsecond versions of ${}_Tg_P$ and ${}_Cg_P$ differ from their 5-arcminute counterparts, there is no significant difference between a 1-arcsecond version of $-{}_Tg_P + {}_Cg_P$ and a 5-arcminute version! This is because the high-frequency differences of between the 1 and 5

Table 8. Statistics for individual series components of ${}_{Tg}{}_P$ for global 1-D FFT using GLOBE_5min (mGal)

	$j = 0$	$j = 1$	$j = 2$	$j = 3$	$j = 4$
$i = 0$	N/A[a]	N/A	N/A	N/A	N/A
$i = 1$	RMS = 27.324 Min = 17.439 Max = 48.448	RMS = 0.371 Min = −0.187 Max = 3.568	RMS = 4.5×10^{-4} Min = -0.8×10^{-4} Max = 0.000	RMS = 1.8×10^{-5} Min = -5.2×10^{-5} Max = 1.5×10^{-7}	RMS = 3.8×10^{-8} Min = -9.5×10^{-16} Max = 1.7×10^{-6}
$i = 2$	RMS = 0.193 Min = −1.255 Max = 1.4×10^{-3}	RMS = 3.2×10^{-4} Min = -1.5×10^{-4} Max = 4.0×10^{-3}	RMS = 2.4×10^{-5} Min = -4.1×10^{-10} Max = 5.5×10^{-4}	RMS = 5.0×10^{-8} Min = -1.7×10^{-6} Max = 3.7×10^{-10}	RMS = 3.1×10^{-9} Min = -1.5×10^{-7} Max = 1.1×10^{-14}
$i = 3$	RMS = 8.5×10^{-5} Min = -7.6×10^{-4} Max = -6.5×10^{-7}	RMS = 1.6×10^{-5} Min = -3.0×10^{-4} Max = 7.9×10^{-6}	RMS = 3.3×10^{-8} Min = -1.9×10^{-13} Max = 9.0×10^{-7}	RMS = 4.0×10^{-9} Min = -2.9×10^{-11} Max = 1.5×10^{-7}	RMS = 1.1×10^{-11} Min = 5.7×10^{-10} Max = 3.6×10^{-17}
$i = 4$	RMS = 4.5×10^{-6} Min = -2.6×10^{-9} Max = 6.7×10^{-5}	RMS = 8.8×10^{-9} Min = -2.0×10^{-7} Max = 4.4×10^{-9}	RMS = 2.9×10^{-9} Min = -9.6×10^{-8} Max = 1.2×10^{-13}	RMS = 6.9×10^{-12} Min = -4.5×10^{-14} Max = 2.8×10^{-10}	RMS = 1.0×10^{-12} Min = -1.5×10^{-17} Max = 5.4×10^{-11}

[a] N/A: not applicable

Table 9. Statistics for individual series components of ${}_{Cg}{}_P$ for global 1-D FFT using GLOBE_5min (mGal)

$j = 0$	$j = 1$	$j = 2$	$j = 3$	$j = 4$
RMS = 27.332 Min = 17.445 Max = 48.468	RMS = 0.370 Min = −0.006 Max = 3.570	RMS = 4.5×10^{-4} Min = -7.6×10^{-3} Max = 0.000	RMS = 1.8×10^{-5} Min = -5.2×10^{-4} Max = 1.7×10^{-8}	RMS = 3.8×10^{-8} Min = -8.9×10^{-16} Max = 1.7×10^{-6}

Table 10. Statistics for individual series components of ${}_TW_{P_0}$ for global 1-D FFT using GLOBE_5min ($m^2\ s^{-2}$)

$i = 0$	$i = 1$	$i = 2$	$i = 3$	$i = 4$
N/A[a]	RMS = 3481.581 Min = 2222.09 Max = 6173.22	RMS = 0.845 Min = 0.513 Max = 1.967	RMS = 2.1×10^{-3} Min = -1.9×10^{-2} Max = 1.5×10^{-5}	RMS = 1.2×10^{-8} Min = 8.8×10^{-9} Max = 3.6×10^{-8}

[a] N/A: not applicable

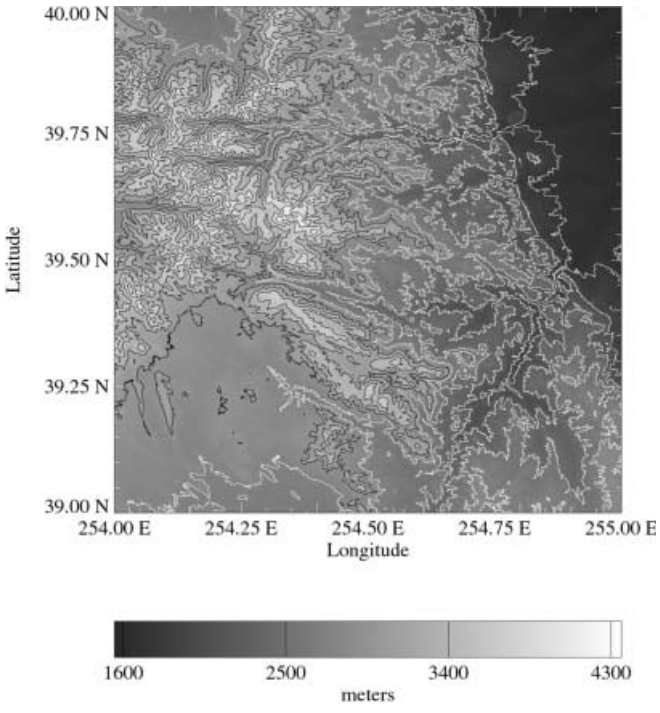

Fig. 15. One-arcsecond topography in a 1 × 1 degree test area of the Rocky Mountains

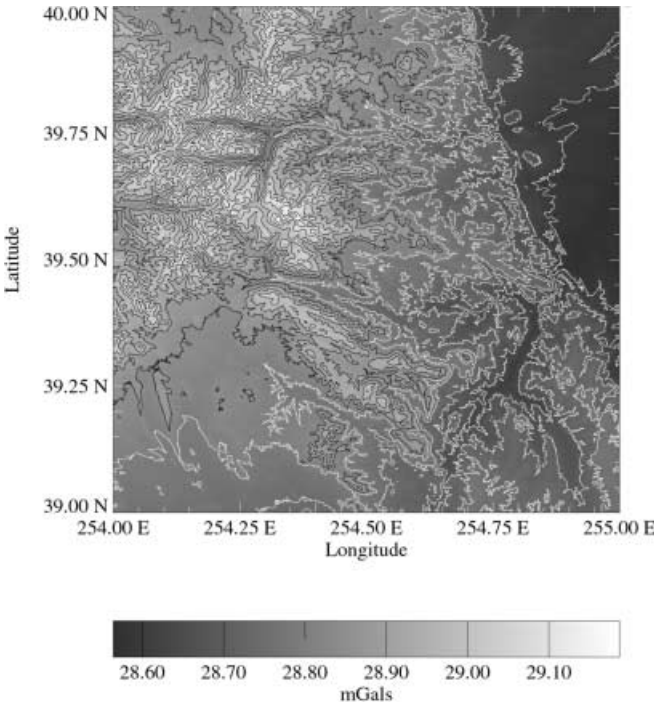

Fig. 16. Gravitational attraction computed at the Earth's surface of 3-D topographic masses outside a 4-degree cap on a 1-arcsecond grid using NGSDEM99 and the ${}_{w}Q_{j}$ procedure

arcsecond versions of ${}_{T}g_{P}$ are almost exactly identical to those same differences in the ${}_{C}g_{P}$ field, causing a cancellation. These statistics are summed up in Table 12. A plot of the '$-{}_{T}g_{P} + {}_{C}g_{P}$' field (at 1-arcsecond spacing) is shown in Fig. 18. This figure is identical to a 5-arcminute version of the same field. Note that the field is very smooth; very long wavelength. While the ease of computing the combined '$-{}_{T}g_{P} + {}_{C}g_{P}$' field at a coarse grid spacing represents an advantage, the smoothness of that combined field is a slight disadvantage. The reason is that very little high-frequency information is removed from the local gravity field, at least based on the outer zone masses. As such, very little is done to 'smooth' the local gravity field due to outer-zone masses, leaving high-frequency information in the local gravity field. This is a disadvantage, as the next step in the R/r/D path is to downward continue. If high-frequency information is left in any field to be downward continued, that signal may become amplified, yielding an extremely noisy field.

The story is a little different in the R/D/r path. In that case, the topographic reduction of $-{}_{T}g_{P}$ is made to surface gravity, and then downward continuation occurs, with $+{}_{C}g_{P_0}$ occurring after downward continuation. Notice in Fig. 16 that the ${}_{T}g_{P}$ field is very high frequency, and since this is removed from the local surface gravity field it means a great deal of smoothing occurs to the local gravity field (and this is based on outer zone masses only!). So while the additional computational burden of computing ${}_{T}g_{P}$ at 1 arcsecond is a disadvantage, the smoothing of the local gravity field before downward continuation is an advantage.

The intent of this comparison is to show that neither path is 'better' than the other. Each has its advantages and disadvantages. However, topographic effects are a direct problem, computable to any accuracy desired within the limitation of DEM spacing and not knowing true rock density. Downward continuation is an inverse problem where small noise can be amplified out of control, therefore requiring various filtering algorithms. Seen in that light, a path which seeks to smooth as much signal as possible out of the field before downward continuation would seem advantageous. That would put the R/D/r path at a slight advantage to the R/r/D path.

Table 11. Statistics of ${}_{TgP}$ and ${}_{CgP}$ computed at 1-arcsecond and 5-arcminute grid intervals in the Rocky Mountain test area

	${}_{T}g_{P}$ (mGal)		${}_{C}g_{P}$ (mGal)	
	1 arcsecond	5 arcminutes	1 arcsecond	5 arcminutes
Average	28.805	28.806	28.981	28.982
Standard deviation	±0.127	±0.121	±0.129	±0.123
RMS	28.806	28.806	28.981	28.982
Minimum	28.564	28.572	28.737	28.744
Maximum	29.187	29.049	29.365	29.226
Number of points	12 967 201	12 967 201	12 967 201	12 967 201

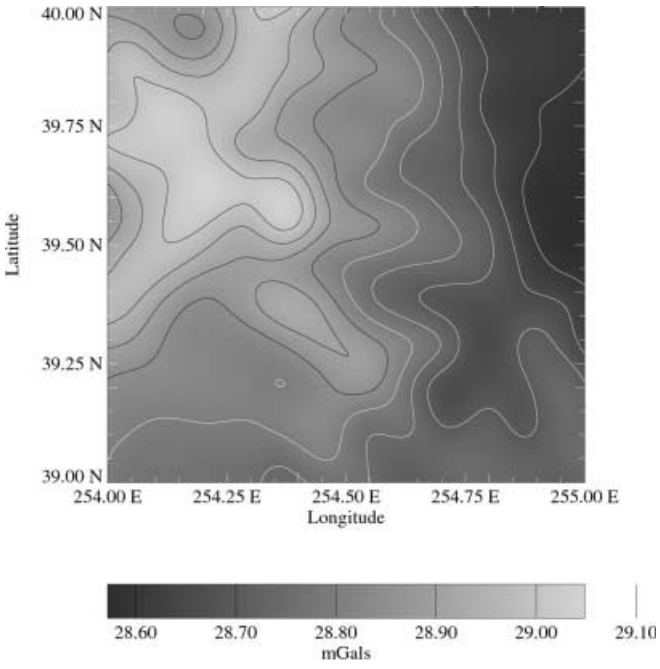

Fig. 17. Gravitational attraction computed at the Earth's surface of 3-D topographic masses outside a 4-degree cap on a 1-arcsecond grid based solely on the GLOBE_5min DEM

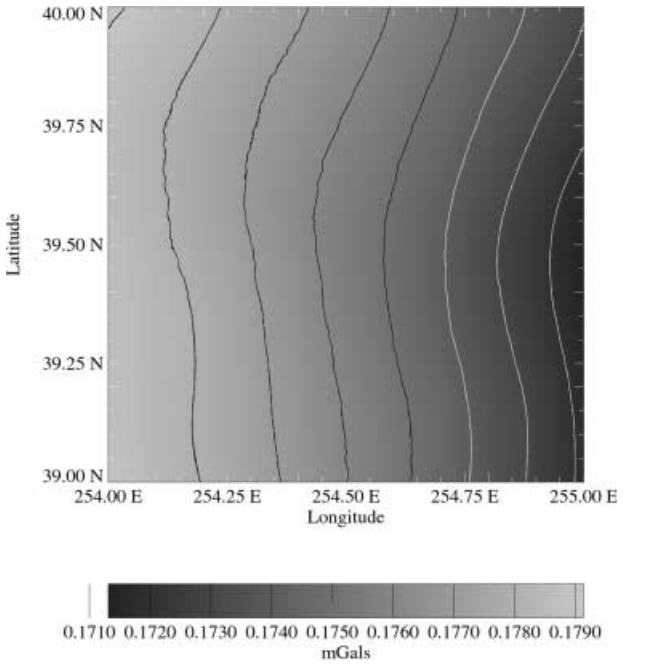

Fig. 18. Combined effect of $-_T g_P + _C g_P$ for topographic masses outside a cap of 4 degrees on a 1-arcsecond grid

7.3 Related computations

Once the ${}_T g_P$, ${}_C g_P$, ${}_C g_{P_0}$, ${}_T W_{P_0}$ and ${}_C W_{P_0}$ values are computed they may be used to compute other useful quantities based on outer-zone masses. Two of these, terrain corrections and indirect effect, are discussed below.

7.3.1 Terrain corrections from outer-zone masses

The traditional terrain correction (TC) approximates the combined effect of $-_T g_P + _C g_{P_0}$. In fact, in planar form the TC is exactly equal to that combined effect (Smith et al. 2001). However, in many local geoid computations the TC is computed only in a local area. Therefore if one examines the outer-zone versions of $-_T g_P + _C g_{P_0}$, an idea of the 'truncation error' of local TC computations becomes obvious (see also Nahavandchi 2000; Sjöberg 2000). Because $-_T g_P$ has a high-frequency signal while $+_C g_{P_0}$ does not (see Sect. 7.1), there is no cancellation of high-frequency terms as was seen with the ${}_T g_P + _C g_P$ signal in Sect. 7.1. That is, truncation error of 'classical' TCs is high frequency. A plot of these truncation errors in the Rocky Mountain test area is shown in Fig. 19. While the effect in this area does not exceed 1 mGal, its systematically negative nature can lead to geoid signals that are greater than 1 cm and should therefore be considered in future geoid computations.

7.3.2 Indirect effect

When the topography is 'Helmertized' the equipotential surface $W = W_0$ moves (generally upward). The distance it moves is the indirect effect. The component of the indirect effect which is caused by the Helmertization of the outer-zone masses may be deduced by applying Bruns' formula (Heiskanen and Moritz 1967), arriving at

$$\delta N_I = \frac{-_T W_{P_0} + _C W_{P_0}}{\gamma_{P_0}} \tag{51}$$

The combined outer-zone grid of $-_T W_{P_0} + _C W_{P_0}$ was divided by normal gravity, g, globally, and the statistics for the global outer-zone indirect effect are shown in Table 13. With an RMS of 2.9 cm and a *minimum* effect of 1.7 cm, it seems obvious that, for a '1-cm geoid', the effect of outer-zone masses must be included in the indirect effect computation.

Table 12. Statistics of $-_{TgP} + _{CgP}$ for 1-arcsecond and 5-arcminute grids and differences (mGal)

	1 arcsecond	5 arcminute → 1 arcsecond	Difference
Average	0.1757	0.1757	6.5×10^{-8}
Standard deviation	±0.0020	±0.0020	$\pm 7.7 \times 10^{-6}$
RMS	0.1757	0.1757	7.7×10^{-6}
Minimum	0.1713	0.1713	-4.4×10^{-5}
Maximum	0.1791	0.1791	3.6×10^{-5}
Number of points	12 967 201	12 967 201	12 967 201

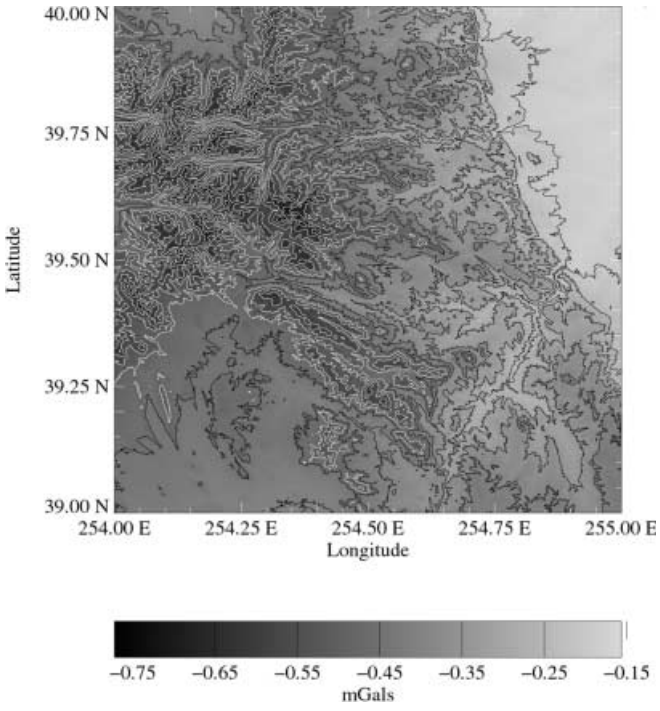

Fig. 19. Combined effect of $-{}_T g_P + {}_C g_{P_0}$ for topographic masses outside a cap of 4 degrees on a 1-arcsecond grid

8 Conclusions

Formulas for computing a global grid of five separate 'outer-zone' topographic effects have been presented, using a 1-D FFT formulation. Various combinations of these topographic effects are needed for different applications of the Stokes–Helmert method of computing geoid undulations. No attempt is made in this paper to compute the inner-zone values, but the implication is that these outer-zone values can be combined (after future research) with inner-zone computations for full topographic effects.

The 1-D FFT method is computationally faster than the numerical quadrature method, while being proven to have similar accuracies. However, a blind application of the derived formulae resulted in numerical errors that needed to be overcome with a special weighting scheme for the kernel function at the cap radius (which, as a matter of course, is necessary in numerical quadrature as well, due to the interaction with a ϕ/λ grid and a circular cap radius). In addition a 5-arcminute grid is recommended to reduce north–south tilts that were evident in 1-degree grid computations.

Two of the five primary functions which were investigated, specifically the gravitational attraction of topography at the surface (${}_T g_P$) and the gravitational attraction of condensed topography at the surface (${}_C g_P$), were seen to have local, high-frequency components due to the dependence on H_p^j terms in their computation. A method for using both a global and local DEM to capture the full signal was proposed with no loss of accuracy and only a quick follow-up computation over and above the global computation. The high-frequency signals of ${}_T g_P$ and ${}_C g_P$ canceled each other in the R/r/D path of the Helmert–Stokes scheme, which was an advantage computationally for the topographic signals but meant that high-frequency signal was not removed from the gravity field before downward continuation. Since the R/D/r path depends on ${}_T g_P$ (and ${}_C g_{P_0}$, rather than ${}_C g_P$, and only after downward continuation), the high-frequency signal is not cancelled, which means it is removed from the gravity field, thus smoothing the field for downward continuation. This is seen as a slight advantage since downward continuation, being an inverse problem, should be done in a field with as much signal (especially high frequency) removed as possible.

Table 13. Global statistics for indirect effects based on topographic masses outside a 4-degree cap (cm)

Average	2.7
Standard deviation	±0.9
RMS	2.9
Minimum	1.7 @ (ϕ, λ) = (−5.208°, 206.5417°), Pacific Ocean
Maximum	6.9 @ (ϕ, λ) = (38.5417°, 83.7083°), Himalayas
Number of points	9 331 200

Lastly, a few examples of magnitude of classical TC and indirect effect signals implied by outer-zone masses were computed. It was seen that the signals, while small, were significant at the few-centimeter level, making them important if an absolute geoid is to be computed to centimeter accuracy.

Appendix

Of academic interest mostly is the question of whether different paths (R/r/D vs R/D/r) from 'Real space' to 'Helmert space' are identical. Intuitively they should seem so (at least mathematically, to the author), but a formal proof of mathematical equivalence is provided here (only an equivalence of R/r/D to R/D/r is provided, but similar elementary proofs of their mathematical equivalence with other paths, such as D/R/r, follow the same structure). Note that a numerical proof and analytical proof is provided for the spherical Earth case by Milbert and Smith (1998), but the following is a proof for the general case.

Also note that a mathematical equivalence does not mean that the practical implementation of R/r/D and R/D/r will yield identical results. Numerical differences, most notably in the computation of the downward continuation, can (if not treated with extreme caution and rigor) yield final values of Helmert gravity that are different through different paths.

First assume the real Earth is divided into two masses I and T, which represent 'masses inside the geoid' and 'topography' respectively. Also, there will eventually be a need to describe a condensed mass layer on the geoid, designated C.

Second, assume there are three 'spaces' (being various configurations of the mass distribution of the Earth) to be considered. The first is the real Earth, designated R. In this case, the Earth consists of the masses I and T. Another

configuration is the 'Helmert space', designated H, where the masses T are missing and have been replaced by the mass layer C. Thus H space consists of masses I and C. Lastly, a midway space, designated M, will be conceived where the only masses in place are the I masses.

Third, define two points P on the surface of the Earth, and P_0, located vertically (along the plumb-line) below P on the geoid. Let h be the distance from P down to P_0.

Lastly, before beginning the proof, a nomenclature needs to be established. The general rule is as follows:

$$\begin{matrix}\langle\text{SPACE}\rangle \\ \langle\text{MASSES}\rangle\end{matrix} \langle\text{variable}\rangle_{\langle\text{LOCATION}\rangle}$$

Where ⟨SPACE⟩ is one of the three spaces, R, M, or H, and is mutually exclusive with ⟨MASSES⟩; ⟨MASSES⟩ is any combination of the three masses I, T, and C, and is mutually exclusive with ⟨SPACE⟩; ⟨LOCATION⟩ is one of two points P or P_0; and ⟨variable⟩ is either g or its derivatives g', g'', etc. Some examples follow.

The gravitational attraction at point P in space H is

$${}^{H}g_P$$

but since H space consists of two masses (I and C), this can be split into the components induced by these two masses

$${}^{H}g_P = {}_{I}g_P + {}_{C}g_P$$

The 2nd derivative of gravitational attraction at point 'P' in space 'R' is

$${}^{R}g''_P$$

but since 'R' space consists of two masses ('I' and 'T'), this can be split into the components induced by these two masses:

$${}^{R}g''_P = {}_{I}g''_P + {}_{T}g''_P$$

The proof of interest is to show that, beginning with gravitational attraction at P in 'R' space (${}^{R}g_P$), the paths R/r/D and R/D/r lead to identical solutions of gravitational attraction at P_0 in 'H' space (${}^{H}g_{P_0}$).

The R/D/r path to ${}^{H}g_{P_0}$ can be written mathematically as

$$\begin{aligned}
{}^{H}g_{P_0} = \quad & \leftarrow \text{target:gravitational attraction at } P_0 \text{ inHelmert space} \\
{}^{R}g_P \quad & \leftarrow \text{begin withattraction at } P \text{ in Real space} \\
-{}_{T}g_P \quad & \leftarrow \text{remove topography (compute at } P) \\
+\sum_{i=0}^{\infty} {}^{M}g_P^{(i)} \cdot \tfrac{1}{i!} \cdot (-h)^i \quad & \leftarrow \text{downward continue } (P \text{ to } P_0) \text{ in mid space} \\
+{}_{C}g_{P_0} \quad & \leftarrow \text{restore condensed topography (compute at } P_0)
\end{aligned} \tag{A4}$$

where the series expansion indicates that downward continuation is done with an infinite Taylor series expansion. However, the R/r/D path to ${}^{H}g_{P_0}$ can be written mathematically as

$$\begin{aligned}
{}^{H}g_{P_0} = \quad & \leftarrow \text{target:gravitational attraction at } P_0 \text{ in Helmertspace} \\
{}^{R}g_P \quad & \leftarrow \text{begin with attractionat } P \text{ in Real space} \\
-{}_{T}g_P \quad & \leftarrow \text{remove topography (computeat } P) \\
+{}_{C}g_P \quad & \leftarrow \text{restore condensedtopography (compute at } P) \\
+\sum_{i=0}^{\infty} {}^{H}g_P^{(i)} \cdot \tfrac{1}{i!} \cdot (-h)^i \quad & \leftarrow \text{downward continue } (P \text{ to } P_0) \text{ in Helmert space}
\end{aligned} \tag{A5}$$

Taking Eq. (A4) and formally showing that 'M' space consists only of 'I' masses in the downward-continuation term, while also expanding the value ${}_{C}g_{P_0}$ into a Taylor series relative to ${}_{C}g_P$, gives

$$\begin{aligned}
&{}^{H}g_{P_0} = \\
&{}^{R}g_P \\
&- {}_{T}g_P \\
&+ \sum_{i=0}^{\infty} {}_{I}g_P^{(i)} \cdot \frac{1}{i!} \cdot (-h)^i \\
&+ {}_{C}g_P + \sum_{i=0}^{\infty} {}_{C}g_P^{(i)} \cdot \frac{1}{i!} \cdot (-h)^i
\end{aligned} \tag{A6}$$

Re-arranging Eq. (A6)

$$\begin{aligned}
&{}^{H}g_{P_0} = \\
&{}^{R}g_P \\
&- {}_{T}g_P \\
&+ {}_{C}g_P \\
&+ \sum_{i=0}^{\infty} \left({}_{I}g_P^{(i)} + {}_{C}g_P^{(i)} \right) \cdot \frac{1}{i!} \cdot (-h)^i
\end{aligned} \tag{A7}$$

Then, recognizing that 'H' space consists of effects of 'I' and 'C' masses, the final term in Eq. (A7) may be simplified, giving

$$\begin{aligned}
&{}^{H}g_{P_0} = \\
&{}^{R}g_P \\
&- {}_{T}g_P \\
&+ {}_{C}g_P \\
&+ \sum_{i=0}^{\infty} {}^{H}g_P^{(i)} \cdot \frac{1}{i!} \cdot (-h)^i
\end{aligned} \tag{A8}$$

Thus Eq. (A8), which is only a re-arranging of the R/D/r path of Eq. (A4), is seen to be identical to Eq. (A5), which was the R/r/D path. The paths yield identical values of ${}^{H}g_{P_0}$. Similar equations can be used to show that other paths are identical, or that equality of target values exists also in potential and gravity gradient space.

Such cases are as intuitive as the preceding proof, and are not presented.

References

Haagmans R, de Min E, van Gelderen M (1993) Fast evaluation of convolution integrals on the sphere using 1-D FFT, and a comparison with existing methods for Stokes' integral. Manuscr Geod 18(5): 227–241

Hastings DA, Dunbar PK (1999) Global Land One-kilometer Base Elevation (GLOBE) digital elevation model, Documentation, vol 1.0. Key to geophysical records documentation (KGRD) 34. National Oceanic and Atmospheric Administration, National Geophysical Data Center, 325 Broadway, Boulder, CO 80303, USA

Heiskanen WA, Moritz H (1967) Physical geodesy. WH Freeman, San Francisco

Li YC, Sideris MG (1994) Improved gravimetric terrain corrections. Geophys J Int 119: 740–752

Martinec Z (1998) Boundary-value problems for gravimetric determination of a precise geoid. Lecture Notes in Earth Sciences, no. 73. Springer, Berlin Heidelberg New York

Martinec Z, Vaníček P, Mainville A, Vronneau M (1996) Evaluation of topographical effects in precise geoid determination from densely sampled heights. J Geod 70(11): 746–754

Milbert DG, Smith DA (1998) Implications of spherical Earth models for gravity reduction procedures and geoid computation. Poster presentation at the Autumn meeting of the American Geophysical Union, San Francisco. Available online at: http://www.ngs.noaa.gov/GEOID

Nahavandchi H (2000) The direct topographical ccorrection in gravimetric geoid determination by the Stokes–Helmert method. J Geod 74(6): 488–496

Nahavandchi H, Sjoberg L (1998) Terrain correction to the power H3 in gravimetric geoid determination. J Geod 72(3): 124–135

Sjöberg LE (2000) Topographic effects by the Stokes–Helmert method of geoid and quasi-geoid determinations. J Geod 74(2): 255–268

Sjöberg LE, Nahavandchi H (1999) On the indirect effect in the Stokes–Helmert method of geoid determination. J Geod 73(2): 87–93

Smith DA, Milbert DG (1999) The GEOID96 high resolution geoid height model for the United States. J Geod 73(5): 219–236

Smith DA, Roman DR (2001a) GEOID99 and G99SSS: one arcminute geoid models for the United States. J Geod 75(9–10): 469–490

Smith DA, Roman DR (2001b) A new high resolution DEM for the Northwest United States. Surv Land Inf Syst 61(2): 103–112

Smith DA, Robertson DR, Milbert DG (2001) Gravitational attraction of local crustal masses in spherical coordinates. J Geod 74(11–12): 783–795

Vaníček P, Huang J, Novk P, Pagiatakis S, Vronneau M, Martinec Z, Featherstone WE (1999) Determination of the boundary values for the Stokes–Helmert problem 73(4): 180–192

Wichiencharoen C (1982) The indirect effects on the computation of geoid undulations. Report 336, Department of Geodetic Science, The Ohio State University, Columbus